Korean J. Chem. Eng., 32(4), 731-742 (2015)
DOI: 10.1007/s11814-014-0290-1

pISSN: 0256-1115
eISSN: 1975-7220

Microscopical characterizations of nanofiltration membranes for the removal of nickel ions from aqueous solution

Oluranti Agboola*,†, Jannie Maree, Richard Mbaya*, Andrei Kolesnikov*, Rotimi Sadiku*, Arne Verliefde***, and Arnout D'Haese*****

*Department of Chemical, Metallurgical and Material Engineering, Faculty of Engineering and the Built Environment, Tshwane University of Technology, Pretoria 0001, South Africa
**Department of Environmental Science and Water Care, Faculty of Science, Tshwane University of Technology, Pretoria 0001, South Africa
***Particle and Interfacial Technology Group, Faculty of Bioscience Engineering, Ghent University, Coupure Links 653, B-9000 Gent, Belgium
(*Received 23 May 2014 • accepted 27 September 2014*)

Abstract−The nanofiltration (NF) process is electrostatically governed and the surface free energy plays a key role in the separation of particulates, macromolecules, and dissolved ionic species. Streaming potential measurement and the surface charge mapping by Kelvin probe atomic force mircoscopy (AFM) have been carried out. Forces of interaction near the surface of nanofiltration membranes were further studied by a force spectroscopy using atomic force microscopy. The two membranes used are more negatively charged at high pH values; hence the higher the solution chemistry, the higher and faster will be adhesion of ions on the surface of the nanofiltration membranes. It was observed that the three acquired signals from non-contact AFM (contact potential difference, amplitude and phase) were rigorously connected to the surface structure of the nanofiltration membranes. In addition to the surface structure (roughness), electrostatic interactions can also enhance initial particle adhesion to surfaces of nanofiltration membranes. The performance of the NF membranes was further investigated for the removal of nickel ions from aqueous solution, and the results were correlated to the mechanical responses of the nanofiltration membranes obtained from AFM and the streaming potential measurement.

Keywords: Nanofiltration Membranes, Streaming Potential, Surface Charge, Atomic Force Microscopy, Forces of Interaction, Amplitude Mode

INTRODUCTION

The physical and chemical properties of nanofiltration membranes are very important in understanding nanofiltration membrane functions. For optimum operation, the membrane has to possess the physical attributes that gives appropriate interactions with solutes in the process stream [1]. The important physical properties are fouling, surface morphology, pore size distribution and electrical double layer interaction. Nanofiltration fouling involves the accumulation and deposition of consistuent in the feed stream on the membrane surface. Electrostatic interaction between the charged surfaces and colloidal particles has been calculated traditionally within the framework of a mean-field pseudo-one-component formulation, known as Derjaguin-Landau-Verwey-Overbeek (DLVO) theory [2]. However, this method only allows for the calculation of some average values of an electrical potential at some unspecified shear plane for materials with surface chemical inhomogeneties or significant roughness [1].

Many studies have been done to investigate the surface properties of membranes by using electrokinetic techniques such as streaming potential measurements [3-7]. Some studies have also dealt with the quantification of membrane surface potential through electrophoretic mobility of nanofiltration membranes from experimental point of view [8-10]. Molecular dynamic simulations have recently clarified the underlying processes from atomistic point of view, and this has allowed them to study the role that cations play on membrane structure and stability [11-13]. Atomic force microscopy has proved to be a very useful technique employed for surface images with sub-nanometric resolution. By imaging membranes with atomic force microscopy, molecular structure and morphological aspect were demonstrated [14-16].

Although streaming potential measurements are the most frequently used for the evaluation of surface charge properties, they have been criticized [17]. According to Brat et al. [17], the results from prior investigations revealed some uncertainty in individual measurement and data scatter because the differences in instrument design and the lack of calibration standard for streaming potential analyzer makes comparison of data among laboratory challenging. An advantage AFM has over streaming potential is that AFM is an advanced physical instrument with high resolution imaging of any surface, which has the novelty of directly measuring the interfacial interaction between a probe and a membrane surface.

Several studies have been conducted in the past two decades to

†To whom correspondence should be addressed.
E-mail: sadikuo@tut.ac.za, funmi2406@gmail.com

identify the different factors involved in the rejection of metal cations by nanofiltration membranes. Akbari and et al. [18] investigated the effect of solution chemistry and the operating conditions on the nanofiltration of acid dyes, using a nano-composite membrane. Their study showed that the rejections of sodium chloride and sodium sulphate were moderate and declined with increasing feed concentration. Also, by changing the pH, the membrane surface and the dyes charge changed as a result of different interactions at different pH values. Dipankar et al. [19] studied the effect of solution chemistry on water softening using charged nanofiltration membranes: the flux declined with increasing ionic concentration of the feed solution. Schäfer et al. [20] investigated the effects of solution chemistry on the retention of low molecular mass acids versus bulk organic matter by nanofiltration. Their results emphasized that the charge and size of the cations and acids are important for separation. Dahmani and Chabene [21] studied the effect of solution chemistry on the performance of a nanofiltration membrane for nickel removal from an aqueous solution. They found that the solution pH, feed concentration and the ionic strength of the solution affected ion rejection and flux. Choo et al. [22] studied the selective removal of cobalt species from simulated nuclear liquid waste with different nanofiltration membranes at different solution pH levels, different cobalt concentrations, and different ion background concentration. Their study provided an insight into the understanding of the relationships between rejections of a target compound (cobalt) and the chemical equilibria of different species in the feed solution during nanofiltration.

On a molecular scale, AFM measurement has allowed the examination of electrical and the forces of interaction on the surface of nanofiltration membranes. Hybrid materials are of particular interest because they combine two or more properties not traditionally present in the same material, such as the combination of electrical/magnetic properties [23].

AFM measurements may generate a number of various artefacts [24], but the non-contact AFM offers unique advantages over the other contemporary scanning probe such as contact AFM and STM. An advantage of amplitude modulation in non-contact AFM is that there is only one feedback loop (the topography feedback loop) compared to three in a frequency modulation (the phase/frequency loop, the amplitude loop, and the topography loop), making the operation and implementation much easier. With the dynamics of atomic force microscopy, the physical background of the materials can be understood by comparing the strength and electrostatic of van der Waals forces [25]. For smooth surfaces, the electrical capacitance between a sphere with radius R and a plane at distance D is given for D/R<1 by:

$$C(D) \approx 2\pi\varepsilon_0 R\left(\ln\frac{R}{D} + 1.843 + \frac{\theta}{63}\right) \quad (1)$$

With the parameter $\theta\varepsilon$ [0,1] and the electrical permittivity ε_0 of the medium within the limit of a small oscillation amplitude, the electrostatic force acting on the tip is proportional to 1/D [26,27] leading to:

$$F_{el}(D) = -\frac{\pi\varepsilon_0 R}{D}\Delta\phi^2 \quad (2)$$

Here, $\Delta\phi$ is the contact potential difference between the tip and sample. In the above expression, a small roughness of tip or sample can prevent mathematical divergence. For large distance, D/R>>1, the electrostatic force can be approximated as

$$F_{el}(D) = -\frac{\pi\varepsilon_0 R^2}{D^2}\Delta\phi^2 \quad (3)$$

Our objective was to investigate the variation of streaming potential and contact potential between the tip and the surface of Nano-Pro-3012 and NF90 using atomic force microscopy technique. This is in an attempt to understand the charges of the nanofiltration membranes and the forces of interaction between the surfaces of the membranes. This will also enable a succinct explanation of the performance of the membranes for the removal of nickel ions from aqueous solution. The discussion and interpretation of the results will be correlated to the mechanical response of the membranes. The reason for studying nickel ion was that nickel is one of the heavy metals (as soluble ions) that are common contaminants of industrial wastewaters and the solubility of nickel sulfide as a function of pH is at pH 12.

MATERIALS AND METHODS

1. Nanofiltration Membrane Characteristics

A composite nanofiltration membrane (Nano-Pro-A 3012) was chosen as representative of a class of membranes which are acid stable in water treatment applications. The two membranes were chosen because Nano-Pro-3012 membrane was based on a surface layer of melamine polyamine on a polyethersulfone support with a molecular weight cut off of 200 Da. NF90 membrane is a polyamide thin film composite membranes with a molecular weight cut off of 250 Da. The operating parameters of the nanofiltration membranes are shown in Table 1 [28]. The operating parameters in Table 1 are given by the manufacturer of the membranes.

2. Sample Preparation

The experiments were conducted with one liter solution containing a nickel sulfate solution ($NiSO_4$) with concentrations of 10 mg/L, 100 mg/L and 500 mg/L. The solution pH was varied; thus 3, 4, 8 and 9 and the effect of ionic strengths (0.01 M of NaCl) on nickel rejection were investigated. The experiments were conducted by using a 1 000-ml dead-end membrane filtration apparatus (Mem-

Table 1. Nanofiltration membranes operating properties

NF membrane	Maximum operating pressure	Minimum operating pressure	Maximum operating temp.	Allowable pH	Minimum recirculation flowrate	Maximum recirculation flowrate
Nano-Pro- 3012	40 Bar (580 psi)	10 Bar (145 psi)	50 °C (122 °F)	0-12	90 L/min (24 gpm)	280 L/min (74 gpm)
NF90	20 Bar (290 psi)	4.8 Bar (70 psi)	45 °C (113 °F)	2-11	1.4 m^3/hr (6 gpm)	3.6 m^3/hr (16 gpm)

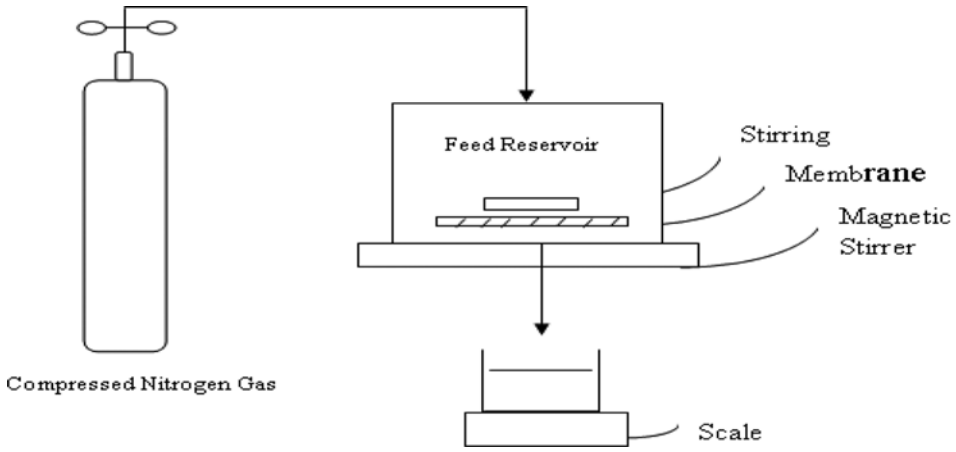

Fig. 1. Schematic diagram of laboratory dead-end filtration system; the complete feed flow is forced through the membrane at a given pressure through nitrogen gas.

con South Africa) with magnetic stirrer. A membrane sheet was fitted to the cell. The membrane active area is about 0.01075 m^2. Operating pressures of 30 and 10 bars were employed via high-pressure regulator and a nitrogen gas cylinder for Nano-Pro-3012 and NF90, respectively. The salts used in preparing the synthetic solutions are analytical grade salts.

3. Laboratory Dead-end Test Cell

The investigation was done using a Memcon laboratory stirring cell as shown in Fig. 1. The membrane tested was placed in the cell. A liter of sample was then placed in the cell at the product inlet. Pressure was then applied with nitrogen gas and the permeate was collected and its mass determined.

4. Analytical Method

Nickel ion concentration was analyzed by using inductively coupled plasma optical emission. Measurements of the solution pH and temperature were made with a pH meter (Mettler Toledo FG20) and thermometer, respectively. The ionic strength was calculated by using a correlation between the conductivity and ionic strength of a NaCl standard, I.S. $[M]=1/2\Sigma C_i Z_i^2$ (C_i is the ion concentration and Z_i is the number of ions).

5. Analysis of Results

Permeate flux and rejections were investigated as function of the working parameters such as operating time and water recovery. The observed rejection, which is the measure of how well a membrane retains a solute, was calculated using Eq. (4).

$$\%R=\left(1-\frac{C_p}{C_i}\right)\times 100 \tag{4}$$

where C_p and C_i are the solution concentrations in the permeate and in the initial feed solution, respectively.

The permeate flux, J_v ($L/m^2/h$), was determined by measuring the volume of permeate collected in a given time interval divided with membrane area, using Eq. (5).

$$J_v=\frac{Q}{A} \tag{5}$$

where Q and A represent flow rate of permeate and the membrane area, respectively.

6. Membrane Characterization

Recent advances in the synthesis and characterization of engineered nanomaterials have brought about new concepts for the design of membranes with increased permeability, selectivity, and resistance to fouling [29-31].

SurPASS electrokinetic analyzer from Anton Paar was used in this investigation. The "SurPASS" instrument, which includes an analyzer, is a measuring cell and a data control system. This instrument measures the streaming potential and streaming current, resulting from the pressure-driven flow of an electrolyte solution that passes through a thin slit channel formed by two identical sample surfaces. The zeta potential of the membranes was determined from the streaming potential measurements. In the experiments, a 0.01 M KCl solution was used; the pH was set in the range 2-8, by adding NaOH and HCl. In the experimental setup, the electrolyte solution is pumped through the cell, which consists of two (of same) membranes with a spacer in between. In this manner, only the charge characteristics on the exterior surface of the membrane are determined. The membrane samples have dimensions of 76 mm×26 mm and are glued onto glass plates. The applied pressure difference was varied between 0.1 and 0.4 bar in order to increase reproducibility. The cell potential was measured continuously by two Pt electrodes. The relationship between the measurable streaming potential, ΔE and the zeta potential, ζ is given by the Helmholtz-Smoluchowski equation (Eq. (6)). Here, E is the streaming potential due to electrolyte flow through a capillary channel, p is the applied pressure driving the flow, ζ is the zeta potential, λ is the electrolyte conductivity, η is the viscosity of the electrolyte solution, ε is the permittivity of the solution (dimensionless) and ε_o is in the permittivity vacuum (fundamental constant). When the valve at the inlet of the cell was closed, the solution stopped flowing through the cell (non-flow mode); the flow started again when the valve was opened (flow mode). The difference in potential between flow and non-flow mode is equal to the streaming potential. This potential difference was measured ten times and a mean value was calculated.

$$\frac{E}{p}=\frac{\varepsilon\varepsilon_o\zeta}{\lambda\eta} \tag{6}$$

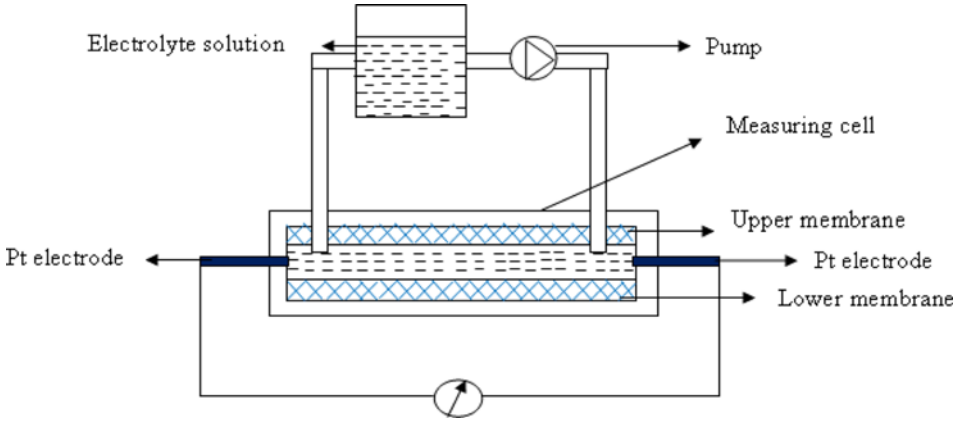

Fig. 2. Functional description of a streaming potential analyzer; this instrument measures the streaming potential and streaming current, resulting from the pressure-driven flow of an electrolyte solution that passes through a thin slit channel, formed by two identical sample surfaces.

The scanning electron microscopy setup used to visualize the surfaces of the membranes was a Joel Field Emission Electron Microscope JESM-7600F. The virgin membranes were mounted on a double-sided carbon tape and the surfaces were coated with iridium (≈5 nm thickness) to make it conductive. The samples were exposed to an electron beam at an accelerating voltage of 15 kV to obtain a signal for the SEM studies. The micro-marker on the micrographs was used to estimate the pore size (diameter).

Clean membrane was cut into small pieces and glued onto a sample holder with an agar tape before non-contact atomic force microscopy imaging was performed using Agilent Technologies 5500 Scanning Probe Microscope (PicoPlus-Atomic Force Microscopy Series 5500). The atomic force microscopy cantilever used was made of silicon (nanosensors) with a resonant frequency of ~60 kHz, a nominal spring constant of 7.4 N/m with a typical tip radius of less than 7 nm. The atomic force microscopy measurements were performed on dry membranes in an air atmosphere with relative humidity of ~30%. The atomic force microscopy images were flattened and the images were analyzed by using the Nanotechnology Research Tool [32].

Force spectroscopy was done with Kelvin Probe Microscopy. WSXM 5.0 software was introduced as a program that can be widely used by the scanning probe microscopy community. It was used to enhance the contrast for the features of interest, providing additional information about the force of interaction near the surface of the membrane [32]. The force-distance curves were obtained with non-contact mode principle, wherein the cantilever is vibrated by an extra piezoelectric transducer. The amplitude of the cantilever oscillations was collected as a function of tip-sample distance, which is the effective distance.

7. Principle of Non Contact Mode

Noncontact mode excites the cantilever at a frequency, $v=w/2\pi$, while the sample is ramped along the Z axis. The cantilever can be modeled as a harmonic oscillator with effective mass, m* and spring constant k_c. The effective mass m* is given by $m^*=m_c+0.24m$, where m_c is the mass of the cantilever and m_t is the mass of the tip. Hence, when the tip is far away from the surface, the equation of motion [33] of the cantilever is given as:

$$m^*\frac{d^2\delta_c(t)}{dt^2}+\gamma\frac{d\delta_c(t)}{dt}+k_c\delta_c(t)=F_0\exp(iwt) \quad (7)$$

where γ is the damping coefficient and $F_0\exp(iwt)$ is the exciting force exerted by the driving piezo-electron transducer on the cantilever. Solving Eq. (4), the "free" amplitude of vibration [29] as a function of frequency is obtained as:

$$A(w)=\delta_c(t)\exp[-i(wt+\phi)]=\frac{F_0}{\gamma w_0}\frac{w_0/w}{\sqrt{1+Q_0^2[(w/w_0)-(w_0/w)]^2}} \quad (8)$$

Here, $w_0=\sqrt{k_c/m^*}$ is the resonance frequency and $Q_0=m^*w_0/\gamma$ is the quality factor. When the cantilever is near the surface, surface forces modify the cantilever vibration and the force $F[D+\delta_c(t)]$, where D is the distance between the sample and the mean position of the cantilever, is to be added in the second term of Eq. (9). The general solution of such an equation cannot be obtained analytically, even when the force law is known. A convenient approximation is the small amplitude approximation, in which the surface force can be written in the form of Eq. (9). Cappella and Dietler [33] followed the derivation by Fontaine et al. [34] to arrive at Eq. (9).

$$F[D+\delta_c(t)]=F(D)+\frac{dF}{dD}\delta_c(t) \quad (9)$$

Using such an approximation, Eq. (9) becomes

$$A(w,D)=\frac{F_0}{\gamma w_0}\frac{w_0'/w}{\sqrt{1+Q(D^2)[(w/w_0'(D))-(w_0'(D)/w)]^2}} \quad (10)$$

With

$$w_0'(D)=w_0\sqrt{1-\frac{1}{k_c}\frac{dF}{dD}} \text{ and } Q(D)=Q_0\frac{w_0'(D)}{w_0} \quad (11)$$

8. Modulation of FM-AFM Frequency

The frequency shift in the frequency-modulation (FM-AFM) can be measured as the output of the phase-locked loop that keeps the phase constant at $-\pi/2$ by adjusting the oscillation frequency [35]. The frequency shift is then used as input for the servo loop

operating the *z-piezo*. An advantage of FM is that the frequency shift gives quantitative information on the force acting between tip and sample [36]. The force in FM-AFM is not directly proportional to the measured frequency shift, but instead to the average force gradient, as can be seen from a simple model. An interaction potential [37] between a tip and a sample was assumed to be denoted by $V_{ts}(z)$. Accordingly, the force is given by $F_{ts}(z)=-dV_{ts}(z)/dz$ and the force gradient by $k_{ts}(z)=-(dF_{ts}(z)/dz)$. If k_{ts} is constant over the range of one oscillation cycle, which is fulfilled, for example, for small amplitudes, the actual resonance frequency, f can be calculated with an effective spring constant, $k+k_{ts}$.

$$f=\frac{1}{2\pi}\sqrt{\frac{k+k_{ts}}{m}} \tag{12}$$

where m is the effective mass and k is the spring constant of the

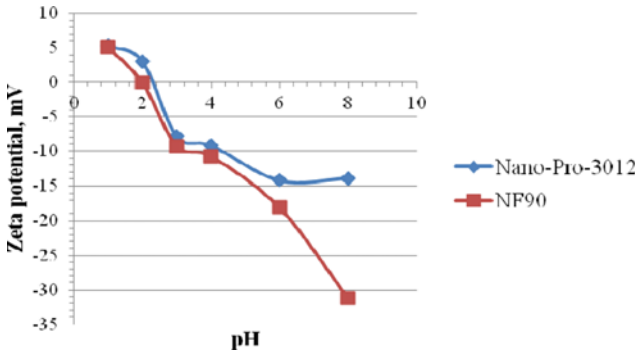

Fig. 3. Zeta potential data of Nano-Pro-3012 and NF90 versus pH. The flow of the electrolyte solution through a channel formed by the membrane generates a streaming current and this leads to a build-up of charge downstream and a potential gradient.

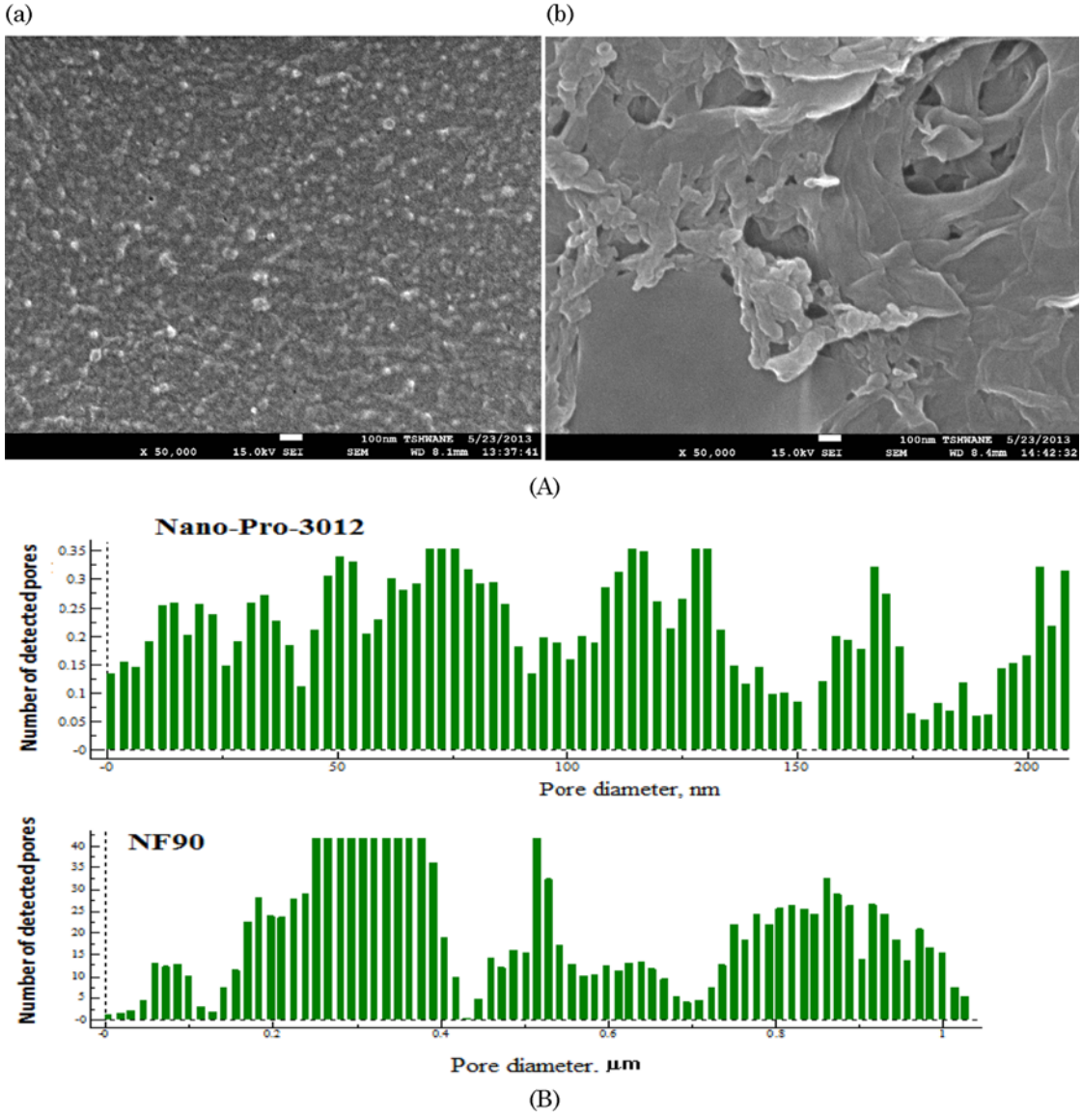

Fig. 4. (A) SEM images of (a) Nano-Pro-3012 and (b) NF90. The structure of Nano-Pro-3012 membrane was dense and compact with few visible pores. NF90 membrane structure shows an intertwined fibrous network with numerous pores. (B) Pore size distribution of Nano-Pro-3012 and NF90, the number of pores detected by NF90 was higher than Nano-Pro-3012.

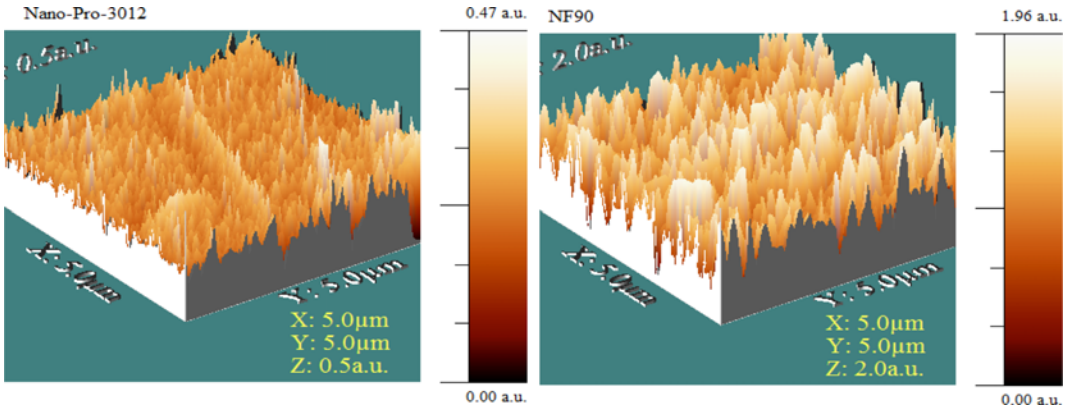

Fig. 5. AFM 3D orthographic image with the vertical scale enhanced in order to amplify the surface morphology of 5.0 μm 5.0 μm Nano-Pro-3012 and NF90.

cantilever. For $k_{is}<<k$, the square root in Eq. (12) can be expanded to enable the calculation of the frequency shift $\Delta f=f-f_0$.

$$\Delta f=\frac{k_{is}}{2k}f_0 \tag{13}$$

When running the FM-AFM with small amplitudes (≤1 nm), a stable and quantitative operation [38] was achieved.

RESULTS AND DISCUSSION

1. Zeta Potential Measurement

Electrical interactions are critically important along and between molecules, at membrane matrix and membrane-surface interfaces. At the nanoscale (e.g., molecular and interfacial regimes), these interactions are associated with electrical dipole or "double layer" charge configurations. Fig. 3 shows the measure of the magnitude of electrostatic interactions between charged surfaces. Nano-Pro-3012 and NF90 are slightly positively charged (zeta potential) at the lowest pH, and they become negatively charged at high pH. The isoelectric point, which is the pH at which the net charge of the membrane is equal to zero, was also observed at pH 2.5 and pH 2 for Nano-Pro-3012 and NF90, respectively. The zeta potential variations of this nature are characteristic of amphoteric surface or surfaces with acidic and basic functional groups, carboxylic and amine groups, respectively [9,37,39,40]. Fig. 2 shows that the two membranes are more negatively charged at high pH values with NF90 (−32 mV) having higher negative charge than Nano-Pro-3012 (−14 mV); hence, the higher the solution chemistry, the higher and faster will be adhesion of ions on the surface of the nanofiltration membranes.

2. Scanning Electron Microscopy

The surface structure of the nanofiltration membranes is shown in Fig. 4(a). Nano-Pro-3012 membrane appears relatively smooth and denser with few visible pores, while NF90 shows intertwined fibrous network with numerous pores. The dense nature of Nano-Pro-3012 shows that Nano-Pro-3012 is not very porous. Pore size distribution is very important for the performance data analysis in membrane technology. It provides a quantitative description of the range of pore sizes present in a given membrane and it gives more accurate description of the particle sizes that is likely to be retained by the membrane. Pore size distribution is one of the numerical parameters that can be obtained directly from atomic force microscopy (AFM). AFM topography imaging of the two membranes was helpful to obtain information on the pore size distribution by giving information on the surface pore dimensions. In comparison, the pore size distribution of the NF90 was higher than the pore size distribution of the Nano-Pro-3012; this shows that NF90 has high porosity (See Fig. 4(b)). Fig. 4(b) shows that the number of pores detected by NF90 was higher than Nano-Pro-3012, this is confirmation that Nano-Pro-3012 is denser. Given that nickel ions are relatively small, the rejection mechanism of nickel ions by these membranes will be explained based on the surface roughness of the membranes in section 3, which is the surface roughness analysis.

3. Surface Roughness Analyses with Atomic Force Microscopy

Fig. 5 shows the non contact mode 3D topography images obtained from AFM for 5.0 μm×5.0 μm neat Nano-Pro-3012 and NF90. The 3D topography images represent the membrane' top views with the information on the depth of the membranes in the Z-direction, coded in color intensity having the highest points. The light regions represent the peaks and the dark region represent the pores. Nano-Pro-3012 has a thick structure and higher ridges of three-dimensional orthographic features. These ridges could be due to manufacturing artefacts that can be useful landmarks when investigating the fouled Nano-Pro-3012, and the thick structure was as a result of the dense nature of the membranes. The 3D orthographic image of NF90 shows the occurrence of tiny peaks and valleys. The tiny peaks of NF90 are responsible for the higher roughness of NF90 when compared to the Nano-Pro-3012. The roughness parameter of the virgin NF90 (355±20 nm) was higher compared to the virgin Nano-Pro-3012 (58±5 nm). The higher roughness leads to greater adhesive strength of the NF90 and greater efficiency in the separation process [41].

4. Surface Charge Mapping by Kelvin Probe AFM

To characterize the potential differences on the membranes, the contact potential difference between the tip and membranes was measured, using the Kelvin probe atomic force microscope. Figs. 6(a) and 7(a) confirmed the result obtained in Fig. 5 with Nano-Pro-3012 membrane having smooth and dense surface with few visible pores and NF90 membrane having structure showing inter-

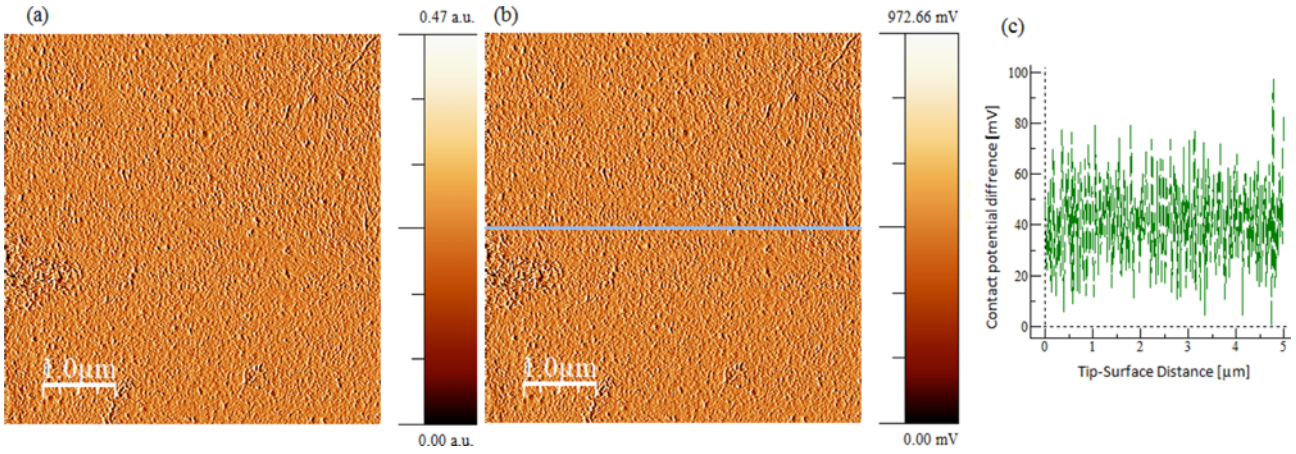

Fig. 6. Surface charge mapping by Kelvin probe AFM of (5×5 μm) of Nano-Pro-3012 (a) topography, (b) contact potential difference across the membrane, (c) cross section through the potential difference.

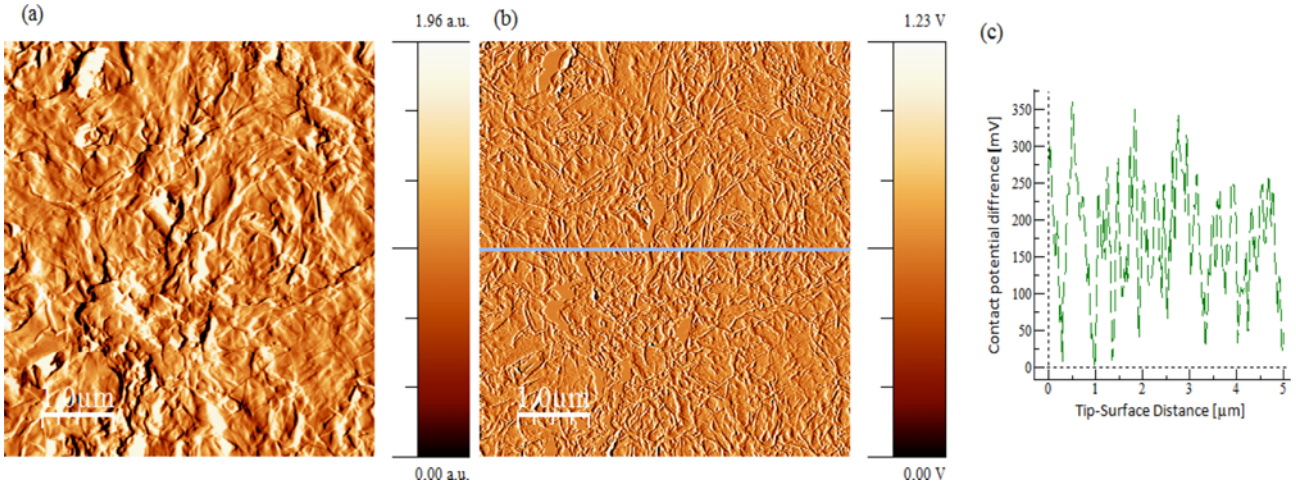

Fig. 7. Surface charge mapping by Kelvin probe AFM of (5×5 μm) of NF90, (a) topography, (b) contact potential difference across the membrane, (c) cross section through the potential difference.

twined fibrous network with numerous pores. Kelvin probe microscopy was used as a second feedback loop to give the tip the same bias potential that the part of the scanned surface had (Figs. 6(b) and 7(b)); thus, the reason why the variation of the surface potential can be measured at every point or section of the membranes (Figs. 6(c) and 7(c)). In Figs. 6(c) and 7(c), the movement of charge varies with distance; the size of the change in potential is proportional to the size of the distance, with NF90 having higher contact potential difference (1.23 V) than Nano-Pro-3012 (972.66 mV-0.973 V). This was as a result of the higher roughness experienced in NF90 (Fig. 5(a)) due to the intertwined fibrous network in NF90. Note that the membrane potential here does not arise from the separation of two electrolyte solutions with different concentrations; therefore, the measured contact potential, in this study only quantitatively corresponds to the charges between the tip and the membranes through mechanical pressure. The strength of contact potential difference between the tip and the membranes directly accompanies the phenomenon of the ionization state and the hydrogen bonding of the interacting group (amphoteric surface or surfaces with acidic and basic functional groups, carboxylic and amine group) observed with the streaming potential measurement. For example, when carboxyl groups are protonated, they have a stronger adhesion with other carboxyl groups in the same ionization state [42]. The streaming potential enabled quantification of the surface charge characteristics. In comparison, the streaming potential of surface is measured based on the voltage developed along the charged surface while electrolyte solution is flowing, whereas the contact potential relies on electron tunnelling in a narrow gap between the tip and the surface of the membranes, where electrons jump from one side to the other through vacuum. Since the current is related to the distance of the tip and the sample, contact potential can be measured. The charge follows a certain function or a correlation to the contact area of the membranes. The movement of charge variations with distance has important implications for the separation mechanisms of nickel ions. It is an indication of surface charge during filtration because the electric charge of nanofiltration membranes is said to be due to the dissociation of functional groups which will enhance the filtration mechanism. The consequences caused by

the difference shown in Figs. 6(c) and 7(c) are as a result of the difference in membrane structure, i.e., pore size.

The charge mapping by Kelvin probe AFM is the ability of the system to acquire and analyze the individual force curves from each tip-sample interaction that occurs during the imaging process. These curves are analyzed in real-time to obtain quantitative mechanical properties of the sample, including adhesion, modulus, deformation, and dissipation. These charge property maps are treated as conventional AFM channels, and can be displayed and analyzed together with topography.

5. Characteristics of Amplitude Mode and Phase Shift

The non-contact amplitude mode and phase imaging are given in Figs. 8(a), 9(a), 10(a) and 11(a). A phase shift represents the amount a wave has shifted horizontally from the original wave, and the amplitude mode is able to measure the surface potential very close to the surface, which greatly improves the lateral resolution of electrostatic forces. The amplitude and the phase imaging give some complementary information to the topography images in Figs. 6(a) and 7(a) by showing the variations in the surface properties of the membranes. The cross section of the amplitude and phase (Figs. 8(b), 9(b), 10(b) and 11(b)) was used to obtain the signals of amplitude and phase. The evolution of the nanofiltration membrane surface morphology was recorded in terms of the tip surface distance from a reference position and the characteristic oscillation, which are the amplitude and phase of the non-contact AFM cantilever (8(b), 9(b), 10(b) and 11(b)).

It was observed that the amplitude signal is sentitive to the nanofiltration membranes surface roughness: the rougher the surface the higher the amplitude. The amplitude signal in this study was found to be the most sentitive to the surface topology of the mem-

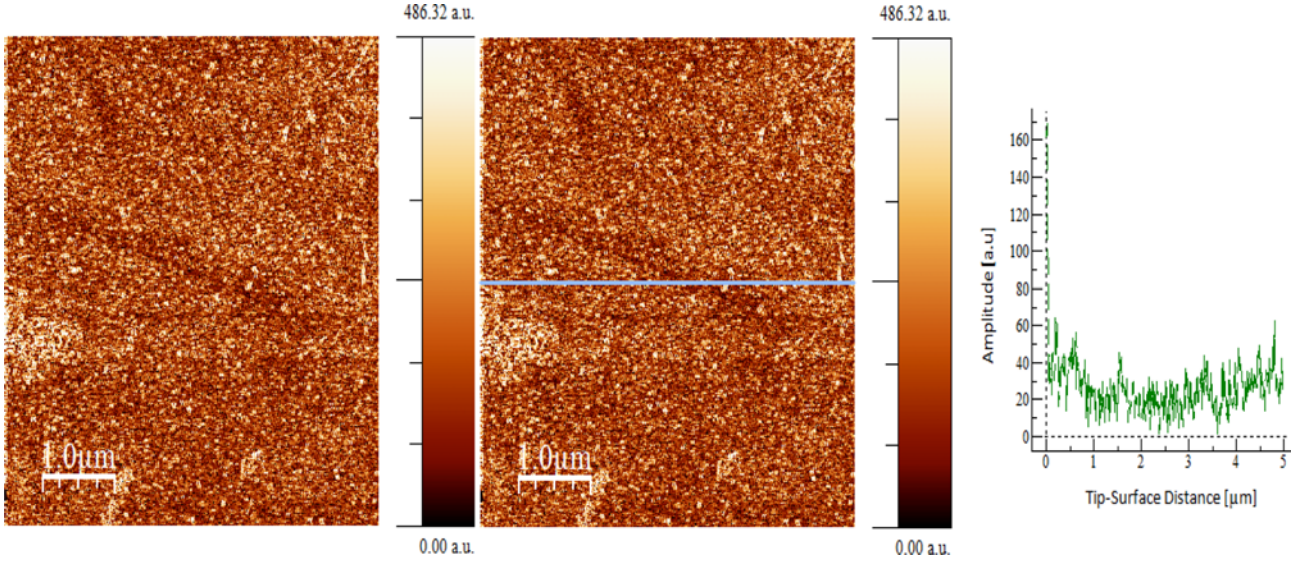

Fig. 8. Conventional non-contact mode of (5×5 μm) Nano-Pro-3012: (a) 2D amplitude image (b) cross section of amplitude image, (c) cross sectional analysis of the amplitude image.

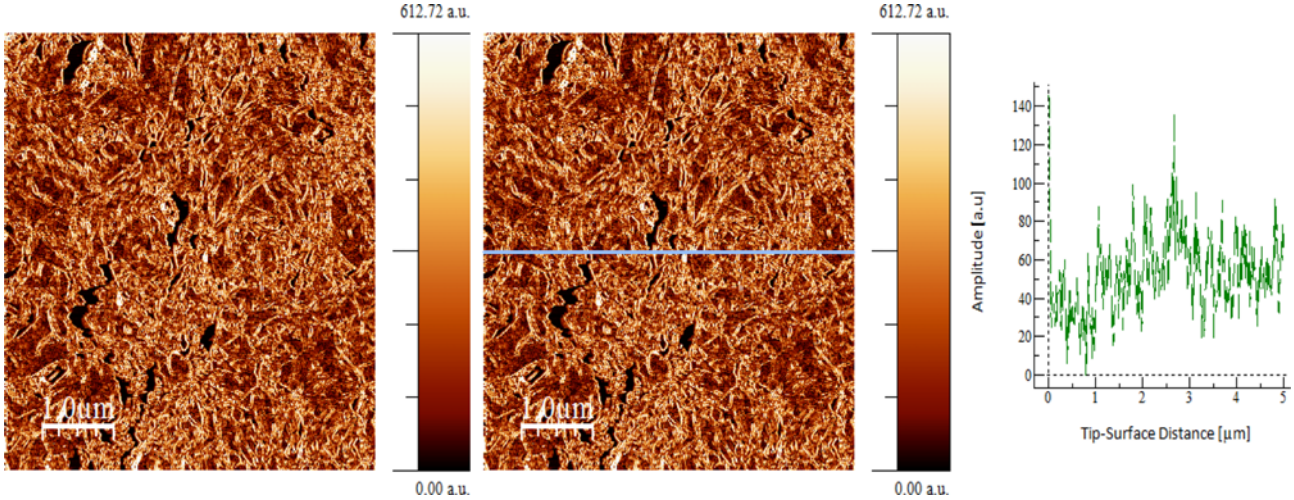

Fig. 9. Conventional non-contact mode of (5×5 μm) NF90: (a) 2D amplitude image (b) cross section of amplitude image, (c) cross sectional analysis of the amplitude image.

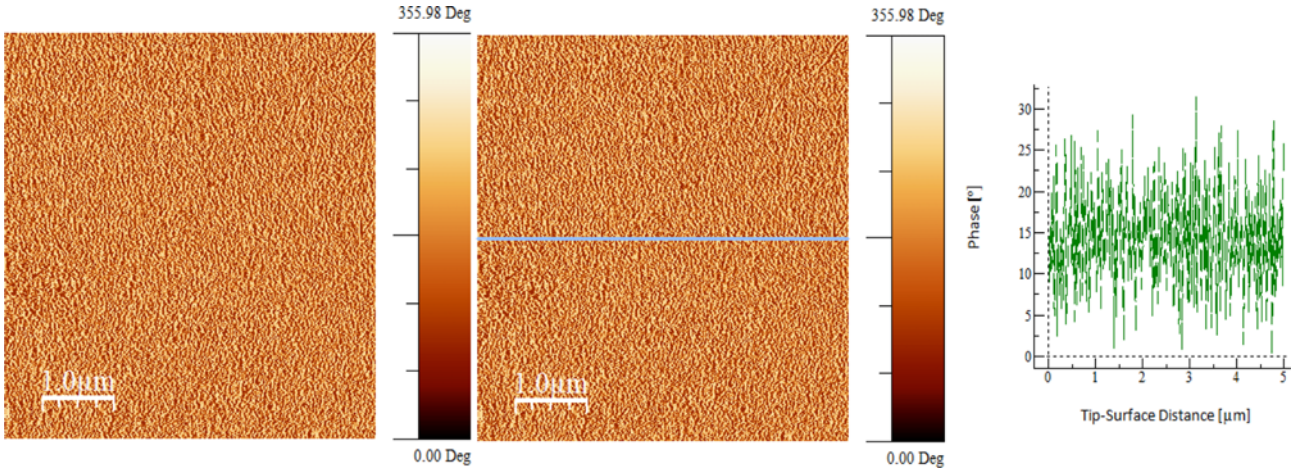

Fig. 10. Conventional non-contact mode of (5×5 μm) Nano-Pro-3012: (a) 2D phase image (b) cross section of phase, (c) cross sectional analysis of the phase image.

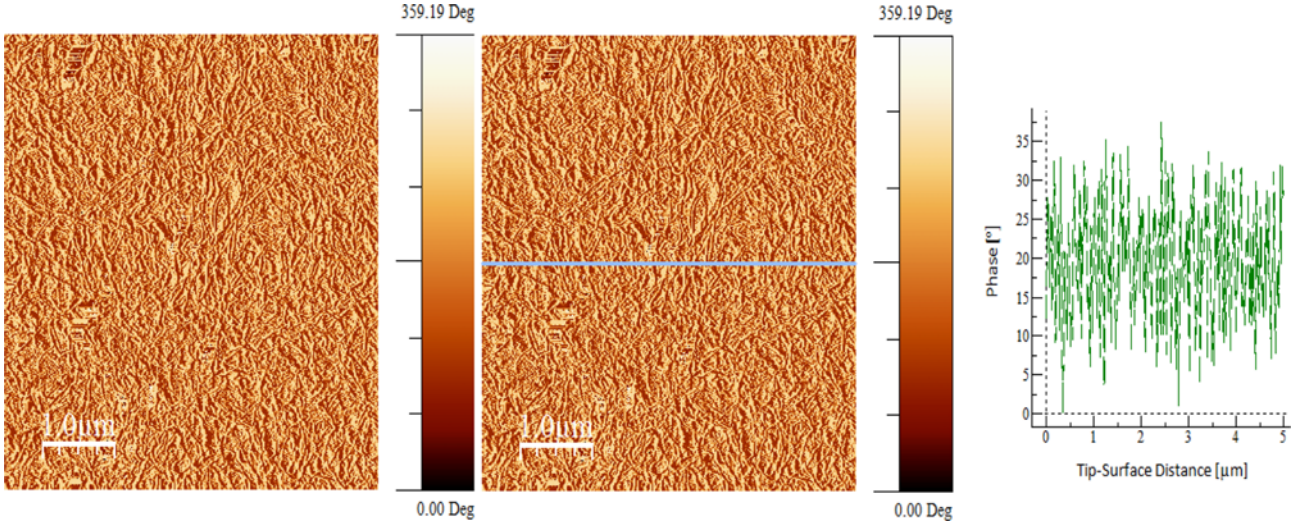

Fig. 11. Conventional non-contact mode of (5×5 μm) NF90: (a) 2D phase image (b) cross section of phase image, (c) cross sectional analysis of the phase image.

branes than the phase. It can be observed from (Figs. 10(c) and 11(c)) that the phase signal changes for the two membranes are due to their mechanical properties (i.e., stress-strain relation and mechanical stability). The results clearly show that the surface charges induced the amplitude and phase signals in the non-contact mode atomic force microscopy. The reason for this effect can be understood from the forces generated by van der Waals and electrostatic interactions; the approximate of relationship in Eqs. (2) and (3) will be added for both forces and the total force acting on a tip [27] is given as:

$$F_{attr}(D) = F_{el}(D) + F_{vdW}(D) = -\left(\pi\varepsilon_0 R^2 \Delta\phi^2 + \frac{HR}{6}\right)\frac{1}{D^2} \quad (14)$$

6. Force Distance Curve

The interpretation of AFM force curves relies almost entirely on established force laws that describe force as a function of the *z*-piezo position. Force measurement was done using atomic force microscopy to further determine the forces generated by van der Waals and electrostatic interactions. Fig. 12 shows that the electrostatic forces depended on the long range distance, i.e., the forces acting on the membrane surfaces were due to the atoms or molecules at the tips. The long-range distance (~350 Å) indicates a length of bridging between membrane samples and the separation tip. The force distance curve obtained here was due to the associated electric field, which originated from a voltage difference across the interfacial contact potential. On approach, the probe detected a slight repulsion, which was likely due to instrument noise, prior to encountering a strong repulsive force. An almost linear increasing force between the tip and the membranes was produced by the repulsive force. The near linear behavior of the approach curve, prior to contact, suggested that a strong repulsive interaction existed between the tip and the membrane surfaces, on close approach.

7. Effect of Feed Concentration, pH and Ionic Background Solution

From the streaming potential measurement, NF90 was more neg-

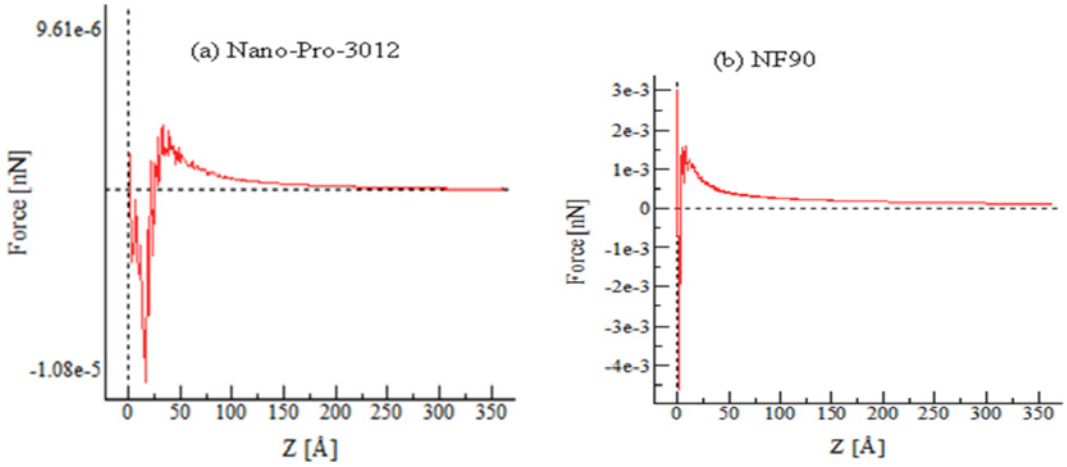

Fig. 12. Force versus effective distance Z [Å]. The probe detected a slight repulsion, which is likely due to instrument noise, prior to encountering a strong repulsive force. The repulsive force produced an almost linear increasing force.

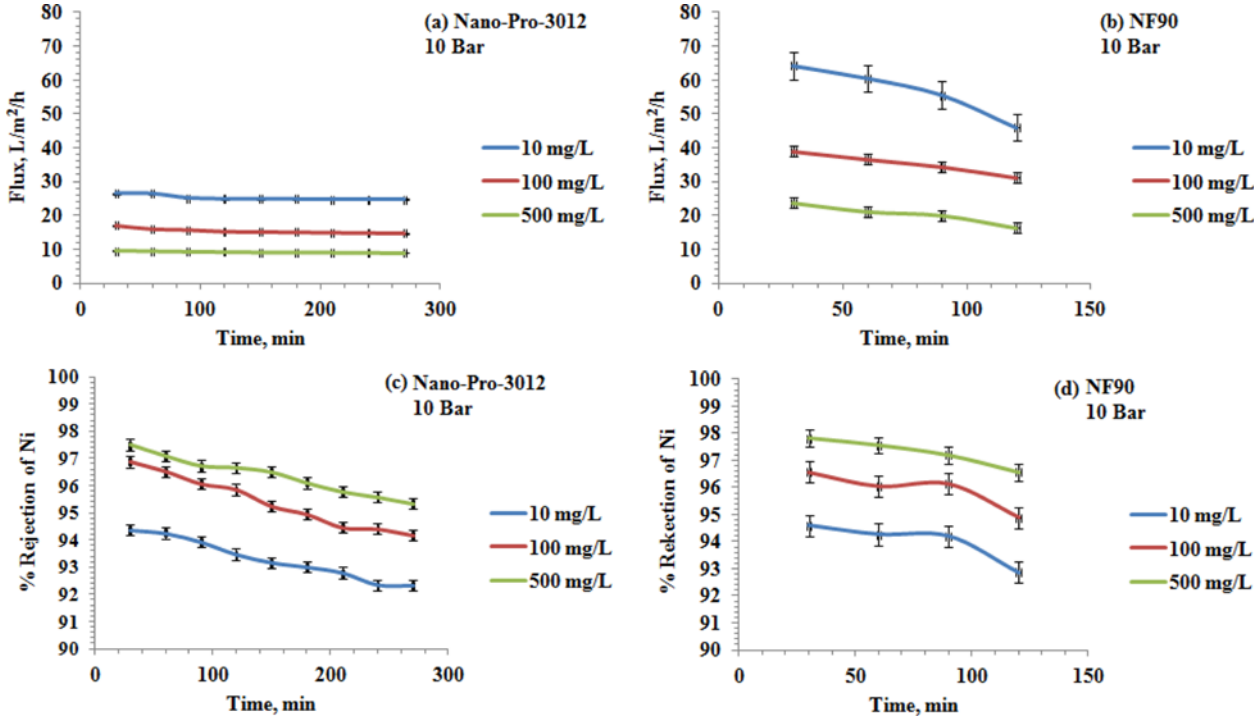

Fig. 13. Effect of feed concentration on the performance of nanofiltration membranes. (a) Flux of Nano-Pro-3012 versus time, (b) flux of NF90 versus time, (c) % rejection of Nano-Pro-3012 versus time and (d) % rejection of NF90 versus time.

atively charged than Nano-Pro-3012. Furthermore, from all the non-contact AFM characterizations, it can be preidcted that NF90 will perform better tha Nano-Pro-3012, due to the following obervations: (1) NF90 has higher roughness which will lead to greater adhesive strength and greater efficiency in the separation process; and (2) NF90 has higher contact potential difference (1.23 V) than Nano-Pro-3012 (972.66 mV-0.973 V), higher amplitude and phase signal than Nano-Pro-3012, due to higher surface roughness. The performance of the two nanofiltration membranes was further investigated for the removal of nickel ions from aqueous solution to correlate the results to the mechanical responses of the nanofiltration membranes, obtained from AFM and the streaming potential measurements.

A clean water flux experiment was done for 2 h to stabilize the membranes before the exposure of the membranes to aqeous solution. It was oberved from Figs. 13(a) and 13(b) that higher concentration of nickel resulted in lower permeate flux due to higher osmotic pressure. The flux decrease with increasing concentration is caused by the adsorption on the membranes [43]. Most of the ions are retained in the feed solution of higher concentration than at lower concentration, thereby resulting in higher rejection at higher concentration (Figs. 13(c) and 13(d); the higher the concentration,

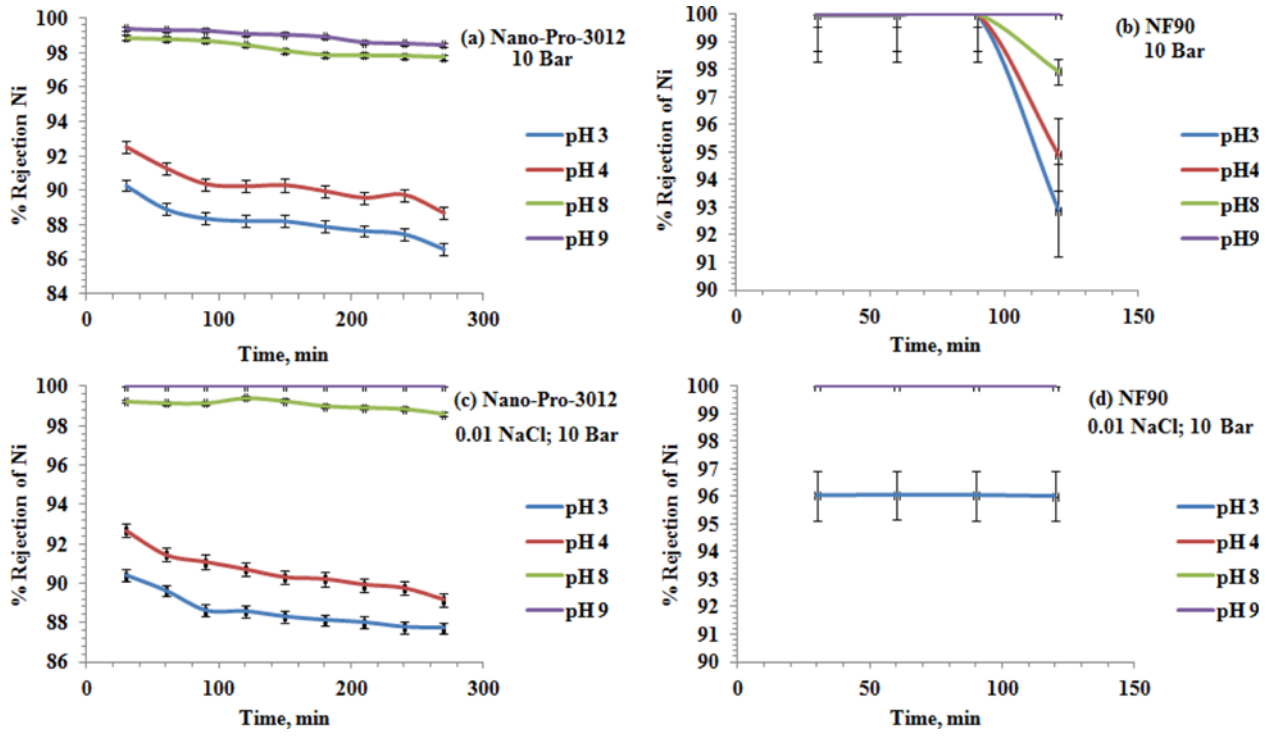

Fig. 14. Effect of pH and background solution on the performance of nanofiltration membranes. (a) % Rejection of Ni by Nano-Pro-3012 versus time at different pH values, (b) % rejection of Ni by NF90 versus time at different pH values, (c) % rejection of Ni by Nano-Pro-3012 versus time at different pH values with the addition of NaCl and (d) % rejection of Ni by NF90 versus time at different pH values with the addition of NaCl.

the higher the rejection; and the lower the concentration the lower the rejection of nickel ions). It was also observed that NF90 had higher rejections for the three concentrations than Nano-Pro-3012; this is because NF90 was more negatively charged that Nano-Pro-3012 (see Fig. 3). Apart from this, NF90 also exhibited higher contact potential difference with respect to the tip separation distance of the AFM (see Figs. 6 and 7).

Figs. 14(a) and 14(b) show that the rejection of Ni ions by the two nanofiltration membranes was higher at higher pH values. This is because the transfer of the unwanted solid particles through the nanofiltration membranes was low at high pH values and high at low pH values. Unwanted solute particles are the ions or contaminants that need to be removed by the membranes. Another explanation to this could be as a result of the increase of pore radii. Pore enlagement could be caused by strong electrostatic repulsions between the dissociated functional groups of the membrane materials [43,44]. This explanation was observed in Fig. 12, whereby a near linear behavior of the approach curve prior to contact suggested that a strong repulsive interaction existed between the tip and the membrane surfaces on close approach. The presence of background ions (NaCl) also influenced the rejection of nickel ions. The impact the addition of NaCl had on the rejection of Ni ions was attributed to the characteristic of the charged membranes, where the forces of repulsion between the negative sites of the nanofiltration membranes and the anions decrease. At this stage, the signal is very weak. The repulsion of anions is very important and this led to higher rejection of nickel ions (Figs. 14(c) and 14(d)). The error bars variations of the experiments are small (they vary from 0.0-1.2).

CONCLUSIONS

A mechanically driven non-contact AFM has successfully provided valuable tools for characterizing the surface charge distribution of nanofiltration membranes. The streaming potential measured the magnitude of electrostatic interactions between charged surfaces. Force distance curve revealed that there is a strong repulsive interaction between the tip and the membrane surfaces. The surface charges actuated the amplitude and phase signals in the non-contact mode atomic force microscopy. This effect can be understood from the forces generated by van der Waals and electrostatic interactions. Experimental results show strong evidence that the potential distribution charges at surfaces of the nanofiltration membranes are due to the surface roughness of the membranes. An understanding of these regimes and the associated cantilever dynamics will guide a rational approach towards selecting appropriate nanofiltration membranes for different waste water processes. Furthermore, the performance of the NF membranes was investigated for the removal of nickel ions from aqueous solution and the results were correlated with the mechanical responses of the nanofiltration membranes. Sometimes the difference in the rejection rate is caused by the membrane structure, which depends on the pH. It is important to know that negatively charged membranes usually exhibit higher rejection rate for charged solutes. The tested experi-

ments of the amplitude modes, phase shift and force distance curve are related to the potential, because the electric charge of nanofiltration membranes is said to be due to the dissociation of functional groups, which will enhance the filtration mechanism.

The novelty of the study is that a new set of experimental data regarding contact potential between the tip and the surface of Nano-Pro-3012 and NF90 using atomic force microscopy technique was used to understand the charges of the nanofiltration membranes and the forces of interaction between the surfaces of the membranes. This enabled a succinct explanation of the performance of the membranes for the removal of nickel ions from aqueous solution.

ACKNOWLEDGEMENTS

The research was financially supported by THRIP and NRF. The authors would also like to acknowledge the University of Pretoria, South Africa, and Ghent University, Belgium, for the laboratory support.

REFERENCES

1. R. W. Bowen, T. A. Doneva and A. G. Stoton, *Colloids Surf., A*, **201**, 73 (2002).
2. P. T. Serrano, S. Yiacoumi and C. Tsouris, *J. Chem. Phys.*, **125**, 1 (2006).
3. I. H. Huisman, G. Trädårdh, C. Trädårdh and A. Pihlajamäki, *J. Membr. Sci.*, **147**, 187 (1998).
4. A. E. Childress and M. Elimelech, *Environ. Sci. Technol.*, **34**, 3710 (2000).
5. M. J. Ariza and J. Benavente, *J. Membr. Sci.*, **190**, 119 (2001).
6. H. Bukšek, T. Luxbacher and I. Petrinic, *Acta Chim. Slovenica*, **57**, 700 (2010).
7. A. Tiraferri and M. A. Elimelech, *J. Membr. Sci.*, **389**, 499 (2012).
8. Y. Shim, H. J. Lee, S. Lee, S. H. Moon and J. Cho, *Environ. Sci. Technol.*, **36**, 3864 (2002).
9. A. E. Childress and M. J. Elimelech, *J. Membr. Sci.*, **119**, 253 (1996).
10. J. A. Brant and A. E. Childress, *J. Membr. Sci.*, **203**, 257 (2002).
11. S. Kaminski and M. A. Mroginski, *J. Phys. Chem. B*, **114**, 16677 (2010).
12. L. Wang, *Molecular dynamics simulations of liquid transport through nanofiltration membranes*, Doctoral dissertation, McMaster University, Ontario, Canada (2012).
13. R. Renou, A. Ghoufi, A. Szymczyk, H. Zhu, J. C. Neyt and P. Malfreyt, *J. Phys. Chem. C*, **117**, 11017 (2013).
14. E. M. Vrijenhoek, S. Hong and M. Elimelech, *J. Membr. Sci.*, **118**, 115 (2001).
15. W. Song, V. Ravindran, B. E. Koel and M. Pirbazari, *J. Membr. Sci.*, **241**, 143 (2004).
16. V. Freger, *Langmuir*, **19**, 4791 (2003).
17. J. A. Brant, K. M. Johnson and A. E. Childress, *J. Membr. Sci.*, **276**, 286 (2006).
18. A. Akbari, M. Homayoonfal and V. Jabbari, *Water Sci. Technol.*, **64**, 2404 (2011).
19. N. Dipankar, T. Kuo-Lun, H. Chi-Chung, C. Ching-Jung, R. Ruoh-Chyu, C. Yan-Che, C. Chih-Shen and W. Tien-Hwa, *Desalination*, **234**, 344 (2008).
20. A. I. Schäfer, A. Pihlajamäki, A. G. Fane, T. D. Waite and M. Nyström, *J. Membr. Sci.*, **242**, 73 (2004).
21. B. Dahmani and M. Chabene, *J. Chem. Eng. Process Technol.*, **2**, 103 (2011).
22. K. H. Choo, D. J. Kwon, K. W. Lee and S. J. Choi, *Environ. Sci. Technol.*, **36**, 1330 (2002).
23. Z. Ji, H. Dong, M. Liu and W. Hu, *Nano Res.*, **2**, 857 (2009).
24. B. Rezek, E. Ukraintsev and A. Kromka, *Nanoscale Res. Lett.*, **6**, 337 (2011).
25. R. Dianoux, F. Martin, F. Marchi, C. Alandi and F. Comin, *J. Chevrier, Phys. Rev. B*, **68**, 454031 (2003).
26. L. Boyer, F. Houze, A. Tonck, J. L. Loubet and J. M. Georges, *J. Phy. D: Appl. Phys.*, **27**, 1504 (1994).
27. H. W. Hao, A. M. Baro and J. J Saenz, *J. Vac. Sci. Technol. B*, **9**, 1323 (1991).
28. O. Agboola, J. Maree, R. Mbaya, C. M. Zvinowanda, G. F. Molelekwa, N. Jullok, B. Van der Bruggen, A. Volodine and C. Van Haesendonck, *Korean J. Chem. Eng.*, **31**(8), 1413 (2014).
29. J. Kim and B. Van der Bruggen, *Environ. Pollut.*, **158**, 2225 (2010).
30. M. M. Pendergast and E. M. V. Hoek, *Energy Environ. Sci.*, **4**, 1946 (2011).
31. C. A. Crock, A. R. Rogensues, W. Shan and V. V. Tarabara, *Water Res.*, **47**, 3984 (2013).
32. I. Horcas, R. Fernandez, J. M. Gomez-Rodriguez, J. Colchero, J. Gomez-Herrero and A. M. Baro, *Rev. Sci. Instrum.*, **78**, 013705 (2007).
33. B. Cappella and G. Dietler, *Surf. Sci. Rep.*, **34**, 1 (1999).
34. P. Fontaine, P. Guenoun and J. A. Daillant, *Rev. Sci. Instrum.*, **68**, 4145 (1997).
35. P. L. T. M. Frederix, P. D. Bosshart and A. Engel, *Biophy. J.*, **96**, 329 (2009).
36. J. Welker, E. IIIek and F. J. Giessibi, *Beilstein J. Nanotechnol.*, **3**, 238 (2012).
37. B. W. Hoogenboom, H. J. Hug, Y. Pellmont, S. Martin and P. L. T. M. Frederix, *Appl. Phys. Lett.*, **88**, 1931091 (2006).
38. T. Fukuma, K. Kobayashi, K. Matsushige and H. Yamada, *Appl. Phys. Lett.*, **88**, 193109 (2005).
39. R. W. Bowen and A. W. Mohammad, *Chem. Engin. Res. Des.*, **76**, 885 (1998).
40. M. Elimelech, W. H. Chen and J. J. Waypa, *Desalination*, **95**, 269 (1994).
41. W. R. Bowen, N. Hilal, R. W. Lovitt and C. J. Wright, *J. Membr. Sci.*, **139**, 269 (1998).
42. J. A. Brant, K. M. Johnson and A. E. Childress, *Colloids Surf., A.*, **280**, 45 (2006).
43. N. M. Sidek, N. Ali and S. A. A. Fauzi, *The governing factors of nanofiltration membranes separation process performance: A review*, Empowering Science, Technology and Innovation Towards Better Tomorrow, *EP33, UMTAS* (2011).
44. P. Berg, G. Hagmeyer and R. Gimbel, *Desalination*, **113**, 205 (1997).